Ceramics International 46 (2020) 1137–1147

Contents lists available at ScienceDirect

Ceramics International

journal homepage: www.elsevier.com/locate/ceramint

Immobilization of doped TiO2 nanostructures with Cu or In inside of macroporous silicon using the solvothermal method: Morphological, structural, optical and functional properties

A. Garzon-Roman[a,b], C. Zuñiga-Islas[a,*], E. Quiroga-González[b,**]

[a] Instituto Nacional de Astrofísica Óptica y Electrónica, INAOE, Luis Enrique Erro 1, 72840, Santa Maria Tonantzintla, Puebla, Mexico
[b] Institute of Physics, Benemérita Universidad Autónoma de Puebla. PO Box J-48, 72570, Puebla, Pue, Mexico

ARTICLE INFO

Keywords:
Porous silicon
Metal assisted chemical etching
TiO_2 structures
Copper and indium dopants
Solvothermal

ABSTRACT

Copper (Cu) and Indium (In) doped titanium dioxide (TiO2) obtained by a solvothermal method was confined in Porous Silicon (PS) prepared by Metal-Assisted Chemical Etching -MACE-, a low-cost and versatile method to investigate the morphological, structural, optical, and electrical properties of the TiO2:X/PS/Si structure (X = In, Cu, 0). According to Scanning Electron Microscopy, different morphologies were found, such as small particles (without dopant) or well-defined geometries such as cubes (indium-doped) and micro-flowers (copper-doped) that covered the PS surface depending on the kind of dopant elements. Cross-section images showed that the TiO2 nanoparticles decorated and filled the macroporous silicon and that they can even form conformal deposits.

Raman spectroscopy and x-ray diffraction patterns revealed the crystalline phase structure of the In and Cu-doped TiO2 materials, which correspond to anatase and rutile, respectively. Furthermore, the lattice parameters corroborated the incorporation of the dopant elements. The photoluminescence (PL) spectra show broad-bands around 2.8 eV, which can be related to oxygen vacancies. Additionally, a blue shift was observed in the PL spectra when the dopant changed from Cu to In. Diffuse reflectance and the Kubelka-Munk plots were used to determine the optical bandgap of the TiO2 structures with and without dopant. Bandgap reduction was observed due to the dopant changes. Current-voltage curves showed a rectifying behavior for negative voltages; however, a negative differential resistance effect was observed for positive voltages in all the samples. Finally, current-voltage curves showed a rectifying behavior for negative voltages; however, it was observed a negative differential resistance effect for positive voltages in all the samples. Besides, these current voltages curves were carried out under dark and illumination conditions, which revealed a photocurrent effect.

1. Introduction

Titanium dioxide (TiO_2) has received enormous attention in the last few years due to its high chemical stability and non-toxic properties [1], excellent optical transmittance, and high photocatalytic efficiency [2].

Moreover, TiO2 has been considered a promising material because of its electrical properties [3], and it can be used in a great variety of applications such as in photodetectors [1], photocatalysis systems [4], gas sensors [5], solar cells [6], lithium battery electrodes [7], and biomedical [8]. Photocatalysis dates back to 1911 when the German chemist Dr. Alexander Eibner integrated the concept in his research of the illumination of zinc oxide (ZnO) on the bleaching of the dark blue pigment, Prussian blue [9] and has been labeled as an effective Advanced Oxidation Process.

Advanced oxidation processes (AOPs) were first proposed in the 1980s [10,11], and involve the in situ generations of powerful oxidation agents such as hydroxyl radicals (OH) to be applied in wastewater treatment [12]. Depending on the means for the creation of hydrolysis radicals, there are many types of AOPs, such as chemical, photochemical, sonochemical, and electrochemical [12]. One of the most common methods that utilize iron salts as the catalyst is the Fenton reaction that produces highly oxidant species [13,14]. In the literature, magnetite structures substituted with transition metals such as niobium and molybdenum have been proposed [13–15] for some AOPs. However, semiconductors such as TiO2 and zinc oxide are the most successful and popular photocatalysts that have demonstrated high

* Corresponding author. Tel.: +52 2224378974.
** Corresponding author.
E-mail address: czuniga@inaoep.mx (C. Zuñiga-Islas).

https://doi.org/10.1016/j.ceramint.2019.09.082
Received 27 May 2019; Received in revised form 5 September 2019; Accepted 8 September 2019
Available online 09 September 2019
0272-8842/

photosensitivity and chemical stability [16].

However, they suffer from some limitations regarding their optical and electronic properties such as high resistance [2,17], wide bandgaps, which limit their use in photochemical applications under visible light irradiation. Even worse, the easy recombination of photo-generated holes and electrons reduces also their efficiency [16]. These properties cause problems for applications in optoelectronics and catalysis. Nevertheless, one-dimensional and multi-dimensional hierarchical structures have demonstrated an improvement in the separation of electron/hole pairs, charge carrier transfer, and enlargement of the active surface area compared to that of TiO2 nanoparticles. This improvement has solved some problems that appear in different applications, mainly in photocatalytic activity [17].

The literature has also reported that TiO_2 doped with transition metals can be a promising strategy to improve the dielectric, ferromagnetic, photocatalytic properties, and an increase in its sensitivity in the visible region [2,18–22].

Also, TiO2, which usually behaves as an n-type semiconductor, can achieve a p-type conductivity due to the substitution of the Ti atom by In Ref. [23]. On the other hand, the use of Cu as a dopant is also crucial because it has high electronic conductivity and can effectively reduce the wide bandgap of TiO2 through the creation of defects and d-band states. This metallic element can also act as active trap centers for electrons and holes to reduce the rate of electron-hole recombination [24]. Moreover, Cu-doped TiO2 has exhibited better efficiencies compared to Au and Ag metal used as dopants [25].

Researchers have studied the inclusion of TiO_2 into semiconductor substrates to improve the photocatalytic activity without altering its optical, electrical, and crystal structure properties [26]. For this purpose porous silicon has been studied as a substrate for these TiO_2 structures, which according to some reports can be promising structures for new technologies in photocatalysis [27], due to the ability of these porous solids to interact with atoms, ions, and molecules in applications that involve ion exchange, adsorption, and catalysis [28].

Even though Uhlir discovered porous silicon (PS) in 1956 [29], it was until 1990 when this material gained attention due to its photoluminescence (PL) in the visible range [30]. Up to now, the study of PS is crucial for applications in optoelectronics, microelectronics, sensors, and medical applications [31,32]. There are many methods to obtain PS layers, but the most important is the electrochemical anodization [30], with which PS layers can be obtained easily in a controlled way. However, Metal-Assisted Chemical Etching (MACE) has gained attention in recent years due to its simplicity and low cost in comparison to the electrochemical anodization that needs the use of an expensive current source. Therefore, the above mentioned we conclude that the combination of metal oxides and PS could result in improvements in the electrical and optical properties for both materials. This improvement in sensitivity has been reported by Baran et al. [33].

This work reports the properties of TiO2 nanostructures doped with Cu and In on PS. Ni/TiO2/PS/Si/Al, Ni/TiO2:In/PS/Si/Al and Ni/TiO2:Cu/PS/Si/Al heterostructures were used to observe the dependence of the morphological, structural, optical and electrical properties on the type of dopant introduced. The synthesis of TiO2 was carried out in one-step using a solvothermal method at a low temperature (180 °C). The incorporation of dopants resulted in extraordinary effects on the TiO2 morphologies, and for that, these results are detailed studied. PS layers were prepared by MACE, which turned out to be an effective method to obtain pores in a controlled way. Also, the electrical properties were evaluated under darkness and illumination conditions finding significant differences. In the I–V characterization, a negative differential resistance (NDR) was observed, and this could be an interesting finding for electronics or optoelectronics applications.

2. Experimental methods

The chemicals used in this work were of reagent grade. Hydrofluoric acid 48% (HF) was provided by MERCK, hydrogen peroxide (H_2O_2), hydrochloric acid (HCl), and methanol (CH_3OH) were provided by J.T. Baker. Silver nitrate ($AgNO_3$), titanium butoxide, and copper chloride ($CuCl_2$) were provided by Sigma-Aldrich and finally, the indium chloride hydrate ($InCl_3H_2O$) was provided by Alfa Aesar.

The MACE method was used to prepare the PS from Si wafers (< 100 > p-type, $\rho = 15–25\,\Omega\,cm$ and $675 \pm 20\,\mu m$ of thickness). Before the chemical etching, the Si wafers were cleaned with deionized water/hydrofluoric acid (HF) (3:1) for 30 s and rinsed with deionized water to remove the native oxide film. Then, the wafers were cleaned in acetone for 5 min in an ultrasonic bath and rinsed again with deionized water, and finally, these wafers were dried with nitrogen. MACE was carried out using as a catalyst, Ag nanoparticles which were deposited on the Si substrates using an AgNO3 aqueous solution of 0.002 M. The plating solution contained 50 ml of the aqueous solution of AgNO3, 1.75 ml of H2O2, and 1 ml of HF (48%). Pieces of Si were immersed in the plating solution for 30 s at room temperature and in an ultrasonic bath. After depositing the Ag nanoparticles, the Si substrates were rinsed with deionized water in order to remove the excess of Ag. Immediately after this process, the Si substrates were immersed in the etching solution for 30 min. This etching solution contained 50 ml of deionized water, 7 ml of H2O2, and 4 ml of HF (48%). After the chemical etching, the PS layers were obtained then, and the wafers were rinsed with deionized water and dried with nitrogen.

On the other hand, TiO2 was synthesized using a similar process reported in Ref. [34] with our modifications. In this case, titanium butoxide was used as the precursor, hydrochloric acid (HCl) as the medium acid, and methanol (CH3OH) was employed as the solvent. In the synthesis, three experimental set-ups were performed. In the first one, 0.083 ml of titanium butoxide were mixed with 1 ml of HCl, and the mixture was dispersed into 10 ml of methanol. The whole mixture was introduced in a 15 ml Teflon-lined autoclave under magnetic stirring for 5 min, then small piece silicon with a PS layer was introduced in the same autoclave. Finally, the system was introduced into the furnace at 180 °C for 4 h. The second experimental set-up was carried out using 0.083 ml of titanium butoxide, and 1 ml of HCl dispersed into 10 ml of methanol together with 6 mMol of copper II chloride (CuCl2) and repeating the same steps as the first experiment. The third set-up was similar to the previous experiments; the only difference was the dopant, which in this case was 6 mMol of indium III chloride dispersed in methanol. After following the above mentioned synthetic procedures to obtain Cu and In doped TiO2, the samples were let to cool at room temperature. Then the samples obtained were rinsed with deionized water and dried with nitrogen. Finally, they were thermally treated at 400 °C for 3 h in order to obtain any of the characteristic phases of TiO2 according to the literature [35,36]. Table 1 lists the samples prepared under different conditions. In order to obtain the electrical characteristics, nickel circular contacts (1 mm diameter and 500 nm of thickness) were deposited on top of the structures whereas Al contacts were deposited at the bottom side of the heterostructures (500 nm of thickness) by high vacuum evaporation. Finally, the structures were thermally treated at 400 °C for 30 min in order to improve the adherence between the sample and the metal contacts. The 400 °C temperature after depositing metals was chosen because it is a typical temperature used to improve the adherence between the metal and the surface; a higher temperature could degrade the structures [37].

The samples were characterized using Field-Emission Scanning

Table 1
Samples prepared under different conditions.

SAMPLE	PRECURSOR SOLUTION	PROPORTION (V:V:V)
PTI15	Titanium butoxide: HCl: Methanol	1:6:60
PTICU	Titanium butoxide: HCl: Methanol:$CuCl_2$	1:6:60 + 6mMol
PTIIN	Titanium butoxide: HCl: Methanol:$InCl_2$	1:6:60 + 6mMol

Electron Microscopy (FE-SEM) using FEI-SCIOS DualBeam equipment operated at 10 kV in order to observe the morphology of the Ag nanoparticles and to analyze in cross-section and top-view the structure of the PS layers before and after depositing the TiO2 material. The elemental composition of the TiO2 structures was determined using an energy-dispersive X-ray (EDX) analysis, which is integrated into the FE-SEM apparatus. Raman spectra of the samples were recorded using a Horiba Raman LabRam HR spectroscopy, with a 632 nm laser, using a 50x magnification. XRD diffractograms were obtained using a Panalytical-Empyrean diffractometer with Cu Kα radiation (λ = 0.15418 nm). The TiO2 powder diffractograms were recorded in the 2θ range from 10° to 70° at a scan rate of 0.017° step size. Room-temperature diffuse reflectance spectra of the heterostructures were measured using a Cary 5000 UV–vis–NIR system (Agilent Technologies Inc., Santa Clara, CA, USA). The reflectance spectra were recorded in a range from 200 to 1500 nm with a resolution of 1 nm. The photoluminescence (PL) response was measured at room temperature using a Horiba Jobin Yvon spectrometer model FluoroMax 3 (Edison, NJ, USA) with a pulsed xenon excitation source and a multiplier tube detector controlled by a computer. The samples were excited using radiation of 330 nm, and the luminescence response was recorded in a range from 370 to 1000 nm with a resolution of 1 nm.

3. Results and discussion

Ag nanoparticles are distributed on the silicon (Si) substrates showing spherical shapes and short-range particle size distribution as can be seen in Fig. 1. The Ag nanoparticles diameter varies from 8 to 34 nm (see the inset image in Fig. 1) the average distance between particles and the etching time generated the formation of macropores, i.e., the micropores collapse among them giving place to bigger pores. This macropores formation will be appreciated in Fig. 2a, where it can be observed both macropores and micropores (these micropores corresponds to the Ag particle size). Something peculiar observed in Fig. 1 is the first pore formation (mesopores) as a result of the process that occurs in the plating solution, i.e., H2O2 is reduced in the presence of Ag particles, liberating holes, which are needed for the etching process (to produce SiO2, which is dissolved by HF) [38,39]. The most accepted mechanism for the deposition of metallic Ag is the oxidation and dissolution of the Si substrate first, and the most suitable mechanism for this is a direct dissolution of Si in a tetravalent state, when the HF reacts

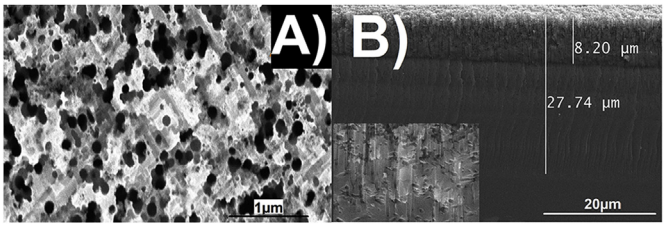

Fig. 2. SEM micrographs of PS layers in a) top-view b) cross-section.

with either Si or SiO2, producing H2SiF6 and liberating electrons. These electrons reduce the Ag + ions from AgNO3 generating Ag0 on the surface of Si substrate [38,39].

Fig. 2 shows a top and several cross-section views of the PS layers synthesized by MACE. A sponge-like structure very similar to the PS obtained using the conventional electrochemical anodization process is observed in Fig. 2a. It is possible to observe a circular geometry in the pore distribution; however, the pore size is bigger than the nanoparticle size, above 100 nm. According to the IUPAC classification, these pores are in the macropore category [40]. The significant difference between the pore and nanoparticle size was mentioned previously, i.e., the average distance among nanoparticles is small, which results in a collapse among the nearest pores generating in this way the macropores. Even if the etching time was longer, these macropores would form bigger pores (as can be appreciated in some regions in Fig. 2a). Therefore, the sizes of pores and those of the particles are quite different. According to Huang et al. [38], the MACE process can be described considering five steps: 1) the oxidant is reduced at the surface of the metal particle. 2) The holes liberated by the reduction of the oxidant diffuse through the metal and are injected into Si. 3) The injected holes oxidize and dissolve the Si atoms at the interface Si/Ag by HF. 4) The concentration of holes is the highest at the interface between Si and metal. Therefore, the Si that is in contact with the Ag metallic is etched much faster by HF than a bare Si surface without metal coverage. 5) The holes diffuse from the Si under the noble metal to off-metal areas or the wall of the pore if the rate of hole consumption at the Si/metal interface is lower than the rate of hole injection. Fig. 2b shows a cross-section of the PS layer where Si channels can be appreciated (the inset image in Fig. 2b shows a zoom-in of this structure). It can be observed in two regions in the PS layer, the first region has a thickness of around 8 µm,

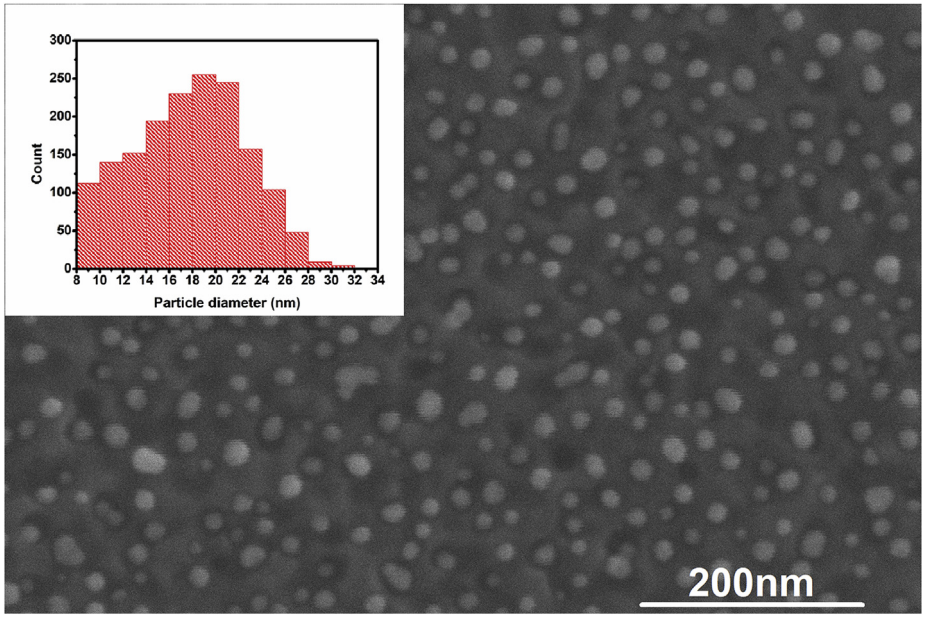

Fig. 1. SEM micrograph of Ag nanoparticles deposited on silicon substrates.

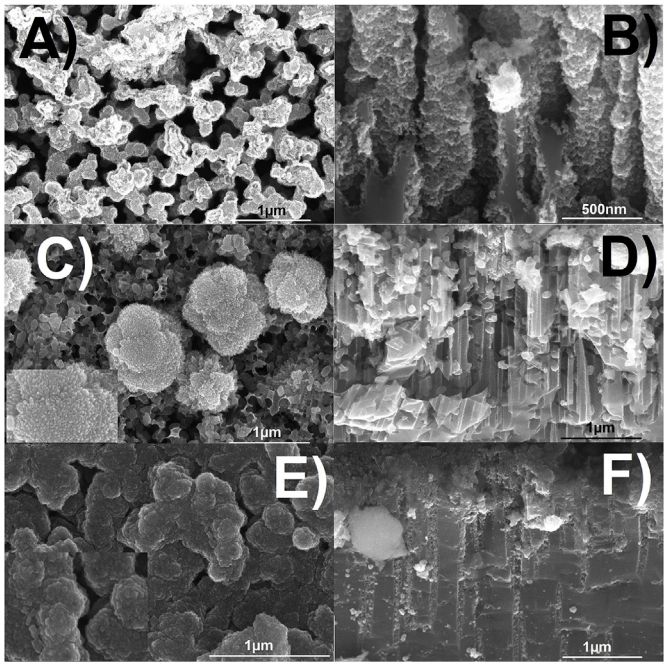

Fig. 3. SEM micrographs in top-view and cross-section of TiO_2 on PS layers a) top-view PTI15, b) cross-section PTI15, c) top-view PTICu, d) cross-section PTICu, e) top-view PTIIn, f) cross-section PTIIn.

and the second region has a thickness of around 20 μm. This phenomenon is rarely seen, and we could attribute it to the nature of the chemical etching since the highest concentration of Ag nanoparticles reach a limit at a specific region where the fifth step previously mentioned is inverted. The total thickness of the porous silicon layers is around 28 μm at 30 min, which indicates that the etching rate is around 0.93 μm per minute.

Fig. 3 shows the PS/TiO2 heterostructure with In and Cu dopants and without any dopant in a top and some cross-section views. Fig. 3a–b shows the TiO2 structures on the PS surface and the coating of the Si channels, respectively. There is a uniform coating on the PS surface with TiO2 nanoparticles around 15 nm of diameter as can be seen in Fig. 3a. Fig. 3b shows the cross-section view confirming a conformal deposit of the TiO2 nanoparticles inside of the pore walls, which sometimes is only achieved by a complex synthesis process such as PECVD [41].

In Figures, 3c and 3d show the PS/TiO2: Cu heterostructures in a top and cross-section views. Fig. 3c displays a radical change in the morphology in comparison with the non-doped sample. In this case, two morphologies can be observed, the first one corresponds to irregular nanoparticles with a similar size to the pores, and therefore, these particles can enter the pores. In the second experiment, the morphology has a peculiar form similar to a cauliflower of micrometric size (as it is shown in the inset image of Fig. 3c). Multiple agglomerations of short nanorods form this structure from the core to the surface. The change of the morphology is due to the segregation of Cu (even at low concentrations) which could be similar to that reported for copper thin films [42]. Fig. 3d shows the cross-section of the heterostructure, and some TiO2 particles inside of the Si channels can be seen. The particle size is similar to the pore size. Therefore, it is difficult to achieve full decoration of the Si channels (as can been seen in Fig. 3b).

Fig. 3e–f shows the PS/TiO2: In heterostructure in top and cross-section views. Fig. 3e shows a similar morphology as in the first case (non-doped). However, there are many changes in morphology. First, the size of these particles increases almost two times; it can be seen in Fig. 3a. Second, by comparing Fig. 3a–e, it can observe that there is a more significant agglomeration in the TiO2: In sample than in pure TiO2, the PS surface seems to disappear because of the coating. Third, the geometry of these particles changes from spherical (non-doped TiO2) to cubic forms (In-doped TiO2 and the inset image in Fig. 3e shows this morphology). The TiO2 structures morphology doped with In are affected as in the Cu-doped TiO2 case. Fig. 3f shows the cross-section of the heterostructure, and it observes how the In-doped TiO2 nanoparticles fill the Si channels. This effect is different in comparison with the non-doped TiO2 sample (which can be considered as a conformal deposit).

The images confirm that the doped radically affects the TiO2 morphology, even if low concentrations are used. Therefore, it could be considered an effective way to modify the morphological properties of the TiO2 instead of changing solvents [34]. Moreover, doped TiO2 structures not only change in their morphology but also in their optical, structural, and electrical properties, and this can be taken to our advantage.

The SEM microscope is also equipped with Energy Dispersive X-ray spectroscopy (EDX) for elemental analysis. EDX analysis confirmed the presence of Cu and In metals in the TiO_2 structures supported in the PS layers. The results are summarized in Table 2.

Fig. 4 shows the Raman spectra of the TiO_2/PS heterostructures with the different dopants used. Raman is a useful analytical technique to identify the phase in the TiO_2 structures tracking the peak position as well as understanding the local change in the structure after the incorporation of dopant ions [24]. A series of peaks were found in the samples these peaks are related to the anatase and rutile phases. The sample PTI15 shows peaks at 146 cm^{-1} (E_g) [43–45], 226.6 cm^{-1} (E_g) [45], 436.6 cm^{-1} (E_g) [44], and 641.7 cm^{-1} (B_{1g}) [43] that characterize anatase and rutile phase. The E_g mode is due to the symmetric stretching vibration of O–Ti–O, and the B_{1g} mode is generated by the symmetric bending vibration of O–Ti–O [24,43].

The sample PTICu in Fig. 4 almost shows the same peak position with a slight shifting as a result of doping. However, it is not possible to observe any secondary peaks related to Cu or its oxide phases, as is reported by Choudhury et al. [24]. These peaks are positioned at 147cm-1 (Eg) [43–45], 228.5 cm-1 (Eg) [45], 434.2 cm-1 (Eg) [44], and 621.2 cm-1 (Eg) [44], which are characteristic of anatase and rutile phases. The incorporation of Cu ions in the heterostructure causes the shifting exhibited in the spectra, which in turn, is due to the difference in the ionic size of both metallic ions, 0.73 Å for Cu2+ and 0.64 Å for the Ti4+. This difference causes a mismatch in the lattice structure. In addition, there is a valence difference between Cu(II) and Ti(IV); this affects the stoichiometry of the Cu-doped TiO2 to maintain the charge neutrality: the generation of oxygen vacancies [24]. In order to understand this effect, Cu2+ ions may substitute the Ti4+ ions, which generates a new bond in the lattice, this new bond could be Cu–O–Ti or

Table 2
Cell parameters, crystallite sizes, and EDX analysis of un-doped and doped TiO_2 structures.

SAMPLE	CELL A = B	PARAMETER (Å) C	CELL VOLUME (Å^3)	CRYSTALLITE SIZE (NM)	ELEMENTS	(ATOMIC %)	DOPANT
					Ti (at%)	O (at%)	Doped
PTI15	3.765	9.456	134.04	8.1	39.21	60.78	0%
PTICU	3.757	9.476	133.75	14.51	40.49	57.51	2% Cu
PTIIN	3.761	9.48	134.09	8.62	44.59	54.41	1% In

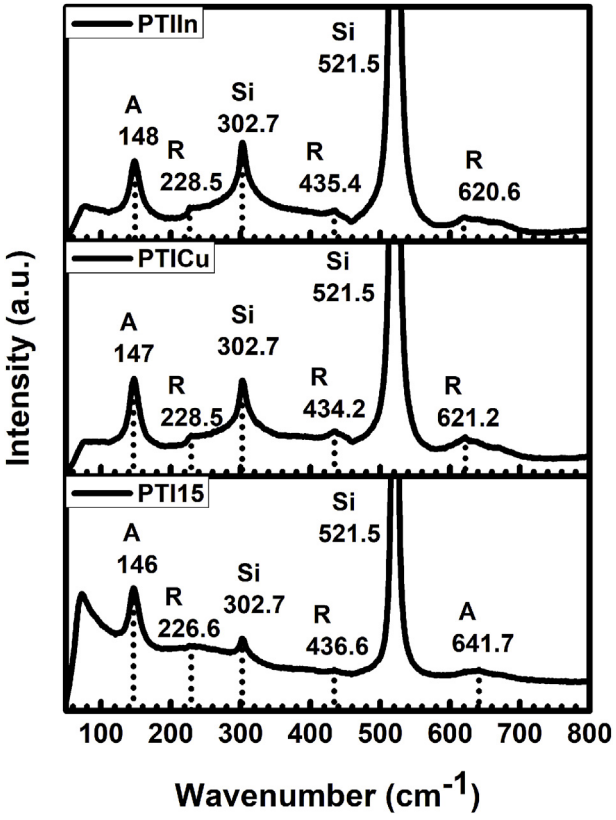

Fig. 4. Raman spectra of TiO_2/PS structures un-doped and with Cu and In dopants.

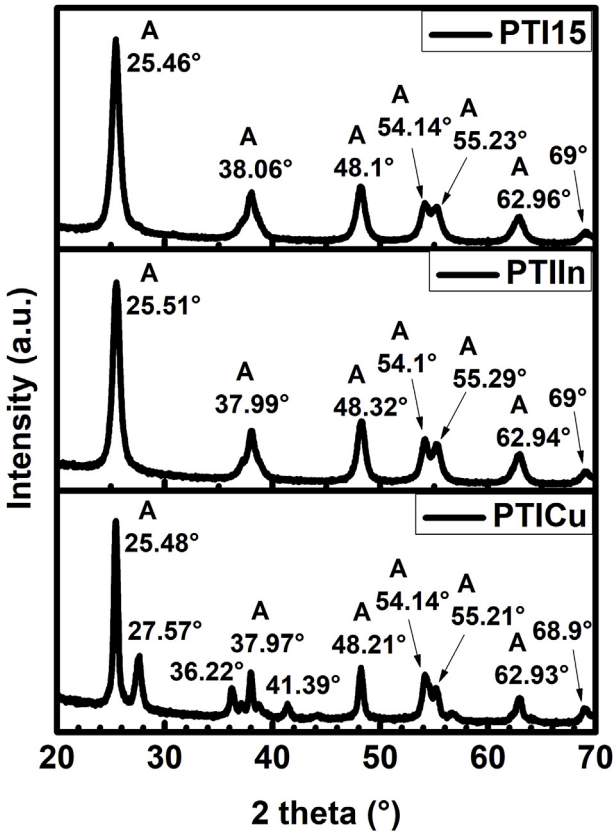

Fig. 5. XRD patterns of In, Cu doped TiO_2 structures and un-doped TiO_2 structures.

Cu–O–Cu as it is claimed by Choudhury et al. [24]. The formation of these bonds will affect the Raman-active modes resulting in the shifting observed in the spectra. Choudhury et al. [24] mentioned that the Eg peak is associated with the Cu–O–Cu stretching mode vibration, and after doping, the vibration strength decreases due to the creation of oxygen vacancies nearby. Then, the lattice contracts due to the oxygen vacancies; therefore, the peak is shifted to a higher wavenumber [24]. However, the quantum size effect has been analyzed, which indicated to be an important parameter in the broadening and peak shifting [24,46].

The sample PTIIn shows shifting peaks around 148 cm-1 (Eg) [43–45], 228.5 cm-1 (Eg) [45], 435.4 cm-1 (Eg) [44], and 620.6 cm-1 (Eg) [44]. These peaks are similar to those reported in the literature, and they are characteristic of the anatase and rutile phases. As in the previous case, it is not possible to observe the presence of the In3+ or its oxide phases, and the only apparent difference is a slight shift of the wavenumbers due to a distortion of the lattice structure. In the substitutional case, when In ions take the place of the Ti ions, new bonds O–In–O are formed, which can be active in the Raman spectrum as a bending mode [47]. The lack of contribution from In–O bonds Raman peaks confirms that many In3+ ions are introduced in the lattice; therefore, a mismatch in the structure is generated, and it is shown as a shift in the Raman peaks. However, Lan et al. [48] concluded that indium ions might exist as some surface species such as O–In-Clx (x = 1 or 2) because the ionic radius of In3+ is larger than that of Ti4+ and there are significant changes in the lattice parameters and cell volume.

On the other hand, all samples have characteristic peaks around 302 cm^{-1} and 521 cm^{-1}. According to the literature, these peaks are assigned to crystalline silicon due to the formation of pores. Also, the peak at 302 cm^{-1} is accounted for due to the formation of silicon nanocrystals embedded in a PS matrix [44].

Fig. 5 shows the XRD patterns of non-doped and doped TiO_2 structures. The non-doped sample PTI15 shows peaks at 25.46°, 38.06°, 48.1°, 54.14°, 55.23°, and 62.96°, which correspond to the (101), (004), (200), (105), (211), and (204) planes confirming the tetragonal anatase phase as reported in the literature [49,50]. However, sometimes it is difficult to differentiate between the anatase peak (101) and the (120), (111) brookite peaks because the 2θ difference between anatase and brookite is only 0.078° [51], and also because the brookite phase disappears at high temperature during annealing [24]. In this study, the thermal annealing was applied in the samples resulting in the elimination of this phase.

The sample PTICu (Cu doped) has almost the same peaks as in the previous case with a slight shifting in 2θ. These peaks are positioned around 25.48°, 37.97°, 48.21°, 54.14°, 55.21°, and 62.93°, which are assigned to the anatase phase. Moreover, other peaks localized at 27.57° (110), 36.22°, and 41.39° can be considered as rutile phase peaks [51]. However, Choudhury et al. [24] consider these peaks as characteristic of the brookite phase, but this does not seem to be logical in our case. Since a thermal annealing was given in these samples; therefore, the brookite phase must disappear.

The PTIIn sample (In doped) shows a shift in the position peaks in a similar fashion to that of the previous sample. The peaks localized around 25.51°, 37.99°, 48.32°, 54.1°, 55.29°, and 62.94° correspond to the anatase phase. All samples have similar peak positions, and the diffraction patterns absence related to compounds derived from Indium or Copper can indicate three possibilities. The first one is that In and Cu ions have been incorporated into the TiO_2 lattice, i.e., there is not a synthesis of In or Cu composites in the TiO_2 structure as is confirmed by Raman spectra. The second one suggests that these species were highly dispersed over the TiO_2 surface, and the third one, probably due to the low concertation of dopant [40]. In the literature [48,49] there is a discussion if the In^{3+} or Cu^{2+} or other ions substitute the Ti^{4+} ion because of the larger radius of these dopant ions (0.81 Å [49], and 0.73 Å [24], respectively) compared to the Ti^{4+} radius (0.68 Å [49]).

Cell parameters, including cell volumes of the TiO2 structures, are summarized in Table 2. These values are comparable to those reported in the literature [49]. The lattice parameters and cell volume for In-doped TiO2 structures show almost the same values in comparison with pure TiO2 structures. Only a slight variation for the "c" parameter is observed; however, it does not confirm if doping has been accomplished. Therefore, we assume that doping by substitutional means can be excluded, and the In metal particles may be present as a surface species or nanocrystals undetectable by XRD. For the Cu-doped TiO2 structures, the cell parameters and the cell volume show a considerable increase. The insertion of the Cu ions that we propose in this case can be due to the similarity between the ionic radiuses. Thus, it can be concluded that Cu ions are introduced in TiO2 in a substitutional mode. Something similar has been reported with Sn ions [48] since the ionic radiuses between Sn and Cu are similar (0.71 Å and 0.73 Å respectively). Hence, we conclude that doping by substitutional mode can surely be achieved with these Cu ions.

Besides, some peaks shift slightly to lower angles, which implies an increase in the interplanar spacing [2]. Moreover, it is possible to observe a decrease in the peak intensity with the use of different dopants. This effect has been explained as a degradation of the crystallinity [2]. Additionally, there is a narrowing of the peaks in the samples doped with Cu and Indium, which may be the result of an increase in the TiO2 crystalline size [49]. This increase in the crystal size of the TiO2 particles has been confirmed by SEM characterization. The crystal size is estimated by using the Sherrer equation based on XRD (101) peaks [24,46]. The crystallite sizes are 8.1 nm, 14.5 nm, and 8.62 nm for PTI15, PTICu, and PTIIn, respectively. The results presented in Table 2 show the different dopants and the effects on the crystal size. These effects were corroborated by SEM images which proved that TiO2: Cu possesses the biggest particles; in contrast, non-doped TiO2 has the smallest particles.

Fig. 6 shows the PL spectra, both the PS layer and doped TiO_2 structures under 330 nm excitation at room temperature. In this case, it is crucial to analyze the behavior of photons generated by electron-hole pair recombination caused by different effects. In general, the PL can be associated with optical recombinations, related to defect levels transitions [23]. In the PS layer, a PL band with a maximum intensity around 1.9 eV (652 nm) and a full width at half maximum (FWHM) around 0.5 eV can be seen.

Different models such as quantum confinement [52,53], hydrogen-termination at nanocrystals [54], oxidized nanocrystals [53,55], localized states [53,55], and structural defects on the surface [56,57] have been proposed in order to explain the origin of PL in porous structures.

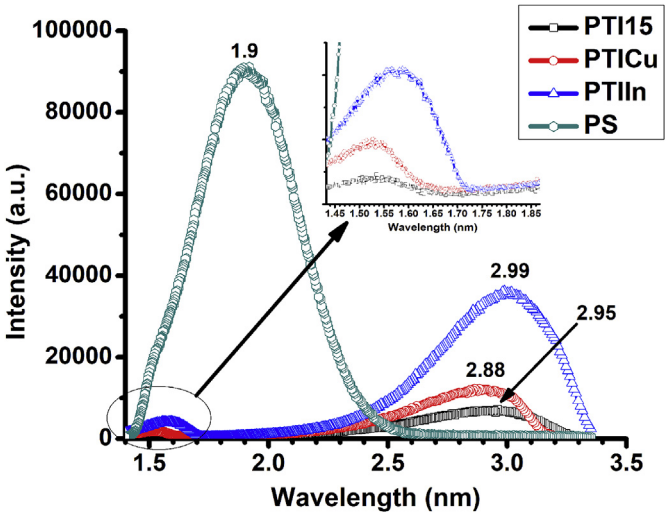

Fig. 6. Photoluminescence spectra of PS layer and Cu and In-doped TiO_2 structures.

In this case, we propose that the PL of the PS layer can be related to quantum confinement and structural defects, since the PS layer can be considered as interconnected Si nanocrystals with different sizes along with a tubular structure [57].

A study performed by Cong et al. [58] reported that the PL peak at 700 nm is due to quantum confinement from silicon nanowires covered by silicon nanocrystals. This Quantum phenomenon can only be observed when the crystalline Si size is comparable with the Bohr radius of excitons in the Si crystals (around 5 nm) [58]. Moreover, in the PL spectrum of the PS layer, a weak shoulder of around 800 nm can be observed, which can be attributed to electron-hole recombinations confined in Si crystals of few nanometers wide [58]. The structural defects are shown in SEM figures (see Fig. 2a), where the PS surface shows roughness and imperfection.

Sanders and Chang [59] proposed a silicon quantum wires model, where four sub-bands in the conduction band and four sub-bands in the valence band close to each other generates multiple peaks and a band broadening that can be observed through a deconvolution process of the spectrum. By using this model [59], the silicon wires can be treated as one-dimensional structures similarly to quantum-wells, where the energy levels can be represented as $E_1 \propto 1/L^2$ L is the size of the well.

Hence, this study proposes that there is a minimum of energy around 8 meV [60] among these sub-bands, which produces an overlay, creating the continuum band effect, as can be appreciated in the PS spectrum of Fig. 6. Also, this effect could originate due to the variation of silicon crystal size; thus, the PL would be a statistical average of the silicon crystal size [60] as it is usually treated for isolated silicon quantum dots [61]. However, it is not possible to discard other effects such as the presence of oxidized nanocrystals, hydrogen-terminated crystals, or defects at the surface, since these three additional effects can be attributed due to the preparation method. Despite this analysis, the PL origin in the PS layer is still unclear.

The PL response before and after depositing TiO2 on the PS layers is shown in Fig. 6. A radical change is displayed in the TiO2 nanostructures confined inside the macroporous silicon layer compared to the pure PS layer. Due to the PL of the PS layer was reduced by the coating of TiO2. This reduction of the PL in the PS layer is a result of a passivation effect due to the coating or decoration of TiO2 on the PS surface, i.e., the TiO2 structures absorb the excitation energy, annulling the PS luminescence. Moreover, there is a blue shifting in all samples with different intensities, as can be observed in Fig. 6. The un-doped TiO2 sample shows a maximum peak of energy around 2.95 eV, while the doped TiO2 structures with Cu and In show the maximum energy peak around 2.88 and 2.99 eV, respectively.

In the literature, the PL spectrum of the TiO2 anatase phase has been divided into three regions for lower energies than 2.65 eV, and the peak is attributed to TiO2 surface states. Medium energies from 2.7 to 2.84 eV correspond to the recombination of photoinduced electrons and holes via the oxygen vacancies with two trapped electrons. Higher energies over 3.01 eV, near to the emission band edge are attributed to indirect transitions [62]. In this case, the PL of our samples seems to be due to the recombination of photoinduced electrons and holes via oxygen vacancies or indirect transitions [62]. According to the literature, the oxygen vacancies are intrinsic defects, and they are created to maintain the charge imbalance [62].

Moreover, these defects seem to be the most important source of the luminescent emission for TiO2, labeled as Vo, Vo+, and Vo++ [63]. The non-doped and doped TiO2 samples possess a similar maximum energy intensity, around 2.9 eV, which could be related to a transition from the oxygen 2p level in the valence band to the oxygen defect level [1] and the variation of the energies must be produced for the dopants inserted in the TiO2 bands. The doped samples have a blue or red-shifting. Due to the possible formation of new bonds, such as Ti–O–In, a new In 5p level is introduced above the oxygen 2p level as an acceptor type level [23].

Something similar could occur with the insertion of Cu dopants

because of the formation of Ti–O–Cu in response to the charge imbalance which arises when Ti4+ is replaced by a lower valence ion (Cu2+); that is compensated by forming an oxygen vacancy. The most stable site for this compensating of oxygen vacancy is the O site, neighboring the Cu dopant in the equatorial position, which has a computed formation energy of −0.35 eV [64]. Additionally, in all samples, an observable broad PL band could also be associated with optical transitions related to anatase and rutile phases [47].

A second weaker visible band around 800 nm could be related to the interaction of the PS layer or be produced due to the rutile phase as Mashary et al. [47] claim (the inset image in Fig. 6 shows a zoom-in of the peak). They mention that the rutile phase usually shows PL bands 1.5 and 1.75 eV, which could be related to possible radiative recombination between midgap trapped electrons and free holes at the valence band. It is not clear what the origin of this band is, despite XRD and Raman characterizations show a contribution of the rutile phase in both samples. Another unexpected fact that is worth to mention is the intensity of the PL spectra, and the PL intensity increases depending on the dopant in comparison with the non-doped TiO2 sample. This effect might indicate that the formation of new bonds and the insertion of new energy levels (caused by metal dopants). These bonds generate an enhancement in the radiative recombination due to an increase in the free carrier concentration [23] and a suppression of photogenerated electron-hole recombination [49].

The energy band gap was determined by using the Kubelka-Munk method and the diffuse reflectance spectra. By using the Kulbelka-Munk method, we determine the bandgap. In the expression from the Kulbelka-Munk method F(R) = (1-R)2/2R, where R is the diffuse reflectance [24]. In this case, F(R) becomes an absorbance function, and the following expression was used in order to determine the bandgap

$$(F(R) * hv)^{\frac{1}{2}} vs \;\; hv$$

To determine the gap, we have extrapolated two lines on the different slopes on the graphs, and the intersection of these lines was the bandgap.

The diffuse reflectance spectra of the samples are shown in Fig. 7a, while the Kubelka-Munk absorption plot is presented in Fig. 7b. The bandgap energies are given in Figures from 7c to 7f. The crystalline silicon possesses the highest reflectance due to the polished surface. The rest of the samples have a considerable reduction in reflectance in all the visible region. Due to the absorption phenomena occurred on the surface of the sample. All samples show the same decreasing tendency as the energy increases. Fig. 7b shows the absorbance function F(R) versus wavelength, and it is apparent to the sight that there are different absorbance bands. The first absorbance band from 250 to 300 nm, can be due to excited electrons, from the valence band to the conduction band, the second band ranges from 350 to 400 nm, and finally the third band ranges from 400 to 750 nm (2B1g to 2 Eg transition [24]), something similar reported by Choudhury et al. [24]. Figures from 7c to 7f show the optical bandgap of the samples. The PS bandgap energy is around 1.65 eV. Otherwise, in TiO2 structures can be appreciated a reduction of the bandgap. The PTI15 sample (Fig. 7f) shows a bandgap around 3.01 eV, which has a different value compared to the already well-known band gap of 3.2 eV for the anatase phase (direct transition from the valence band of the oxygen 2p level to the conduction band of the Ti 3d level [1]).

The PTICu sample (Fig. 7d) has a bandgap around 2.95 eV that can be attributed to the insertion of the Cu^{2+} dopants and oxygen defects, which form sub-bands states in the TiO_2 bandgap. Thus, in the Cu-doped TiO_2, the electrons can be excited in order to make a direct transition or to occupy Cu^{2+} s-d states, and the oxygen vacancies capture electrons [24]. The oxygen vacancy states such as F+ (single electron) and F++ (devoid electron) are responsible for the capture of electrons. Therefore, the sub-band states of Cu^{2+} and oxygen defects are responsible for the reduction of the bandgap of TiO_2 [24].

The PTIIn sample (Fig. 7e) has a bandgap around 2.92 eV that can be related to the introduction of the In 5p level or to an oxygen level defect, as previously mentioned. The reduction of the bandgap for doped samples indicates the insertion of different levels inside of the TiO_2 bandgap. Moreover, the bandgap reduction can be controlled by the surface of the nanostructures, lattice strain, and vacancies [24].

On the other hand, it is possible to determine the width of the defect bands in the TiO_2 bandgap employing the Urbach energy (E_u). This energy is related to the Urbach tail, which refers to the creation of a band tail due to defect states, which extends far down the bandgap from the lower part of the conduction band, and similarly, the defect states near the valence band localized in edge deep inside the gap [24]. The reciprocal of the slopes of the linear portion, below the optical bandgap, gives the value of E_u [24]. Fig. 8d shows the Urbach energy of the samples. The Urbach energies are 69.5 meV and 83.2 meV, for PTICu, and PTIIn, respectively. The results of the Urbach energy values reduce the TiO2 bandgap, due to the introduction of defect levels, similarly reported by Choudhury et al. [24].

Fig. 8 shows the electrical characterization of the heterostructures under illumination and darkness conditions. Heterostructures were evaluated from negative to positive voltages. Fig. 8a corresponds to Ni/PS/Si/Al heterostructures at positive voltage applied, and the PS layers are ruling the current due to its high resistivity since the pores work as charge carrier traps [62].

When the heterostructure is polarized, a depletion region is formed between the Ni contact and the PS layer due to the electrons passing through from the Ni contact to the PS layer, then these electrons travel a certain distance until they recombine with holes, which creates a negative charge on top the PS layer, meanwhile, the Ni contact is positively charged [62].

On the other hand, when a negative sweep voltage is applied, there is a behavior similar to the Zener diode or avalanche diode after applying 40V (this voltage can be considered as a break-down voltage). The saturation current can be obtained from the $J_T \propto J_o \exp(A)$, where J_T is the total current density, and A is a term related to the applied voltage, built-in voltage, and thermal voltage. Thus the saturation current (J_o) has been determined by the extrapolation of the linear region of $Ln(J_T)$, which gives a saturation current around 0.31 μA and 2.9 μA for darkness and illumination conditions, respectively. This significant difference is related to the increase of the slope due to the photoinduced current.

Regarding the different conditions of excitation, it is clear to see a difference between the curve under darkness and illumination. For positive voltages, white light pulses are being applied, a photoresponse can be observed, and an increase in the slope can be observed. Also, for negative voltages, an increase in the breakdown voltage can be observed when light is applied. The explanation for the different current observed is given below: the forward current is generated due to the flow of minority carriers, and the applied voltage injects minority carriers, meanwhile, the reverse current is generated due to the flow of majority carriers [63]. The reverse and forward currents increase exponentially with more voltage applied, which indicates that a diffusion current is dominating in the heterojunction [64,65].

Fig. 8b shows the electrical behavior of the Ni/TiO2/PS/Si/Al heterostructure. In this curve, different defects, both positive and negative voltages, are shown. For negative voltages, it can be observed that after −15 V, the curves start to show current defects. These defects could be related to the internal structure of the heterojunction (traps in the material or oxygen vacancies) or even environmental conditions such as temperature, pressure, mechanical noise; however, it is not clear why this phenomenon occurs. The most interesting effect appears for positive voltages, where a reduction of the current is observed as the voltage increases, this effect occurs at around 1.5 V and is considered as a negative differential resistance (NDR) [66,67] (the inset image in Fig. 8b shows a better image to appreciate this effect). The NDR effect has been widely studied in order to try to explain its origin; models such

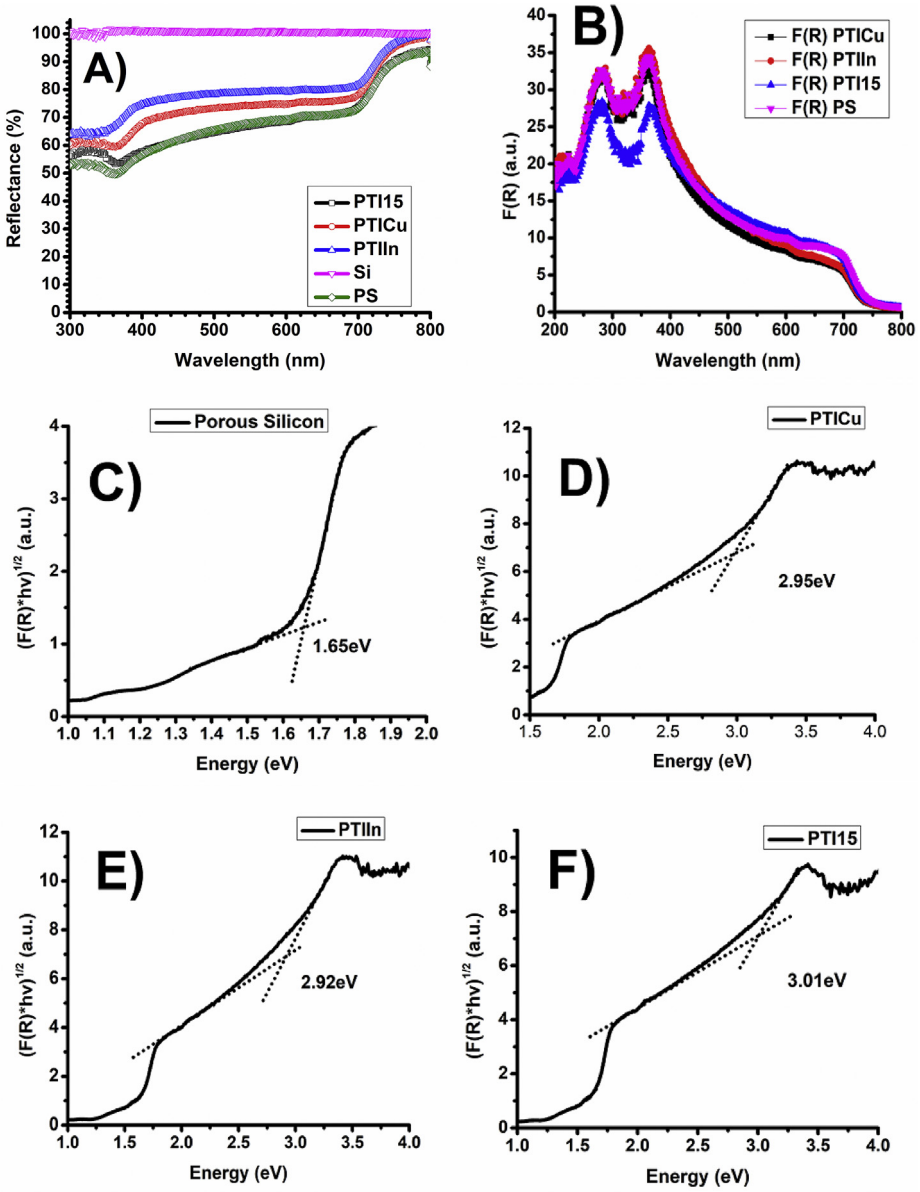

Fig. 7. Diffuse reflectance of the Cu and In TiO_2 structures and Kubelka-Munk method to determine the band gap a) Diffuse reflectance spectra of PS layer and doped TiO_2 structures b) Kubelka-Munk absorption c) determination of gap for PS d) determination of gap for PTICu e) determination of gap for PTIIn f) determination of gap for PTI15.

as tunneling, Coulomb blockade, and charge storage have been suggested as the leading causes for this effect [66].

Fig. 8c and d shows the I–V curves of the Ni/TiO2: Cu/PS/Si/Al and Ni/TiO2: In/PS/Si/Al heterostructures under darkness and illumination conditions. These figures show a considerable difference in comparison with the non-doped structure. First, the negative voltage region increases exponentially in both samples until it reaches the current compliance (10 mA) at low voltages (~ 6 V). It is unknown why this fast increment only appears in these samples (8c and 8d); it is probably due to the introduction of dopants. For positive voltages the NDR effect can be observed for both samples; however, for PTICu after the first current drop, it is possible to see a wave-like effect with a certain periodicity, which could be a contribution of the NDR effect.

On the other hand, the PTIIn sample shows a wave-like effect with random behavior as signal noise. This wave-like effect could originate from the dopants with the introduction of new levels that capture electrons. As it was previously mentioned, the NDR effect could be caused by a different mechanism. For example, resonant tunneling occurs when the quantized states in the quantum well cannot contribute to the coherent tunneling through the double-barrier structure [68] or localized states. These localized atomic states in a sharp structure arising from the tip density of states (DOS) to the metal [69]. Marin et al. [66] mention that the NDR effect appears when conduction channels are blockage due to carrier trapping phenomena in the SiO2/Si interface. These traps capture electrons, which cause a Coulomb repulsion.

Charge storage was reported by Du et al. [70]. Who proposed that the NDR effect is caused due to molecular dimensions in the interface insulator-metal. The exponential behavior of the current indicates electron tunneling. This phenomenon can explain by resistive switching (in our case the TiO2 structures are highly resistive compared with the crystalline silicon or porous silicon) model based on charge trapping and de-trapping introduced by oxygen vacancies in a bandgap state, with molecular oxygen ions as the active source in charge storage.

Charge storage seems to be the most acceptable model for the origin for this NDR effect, based on the evidence obtained from the

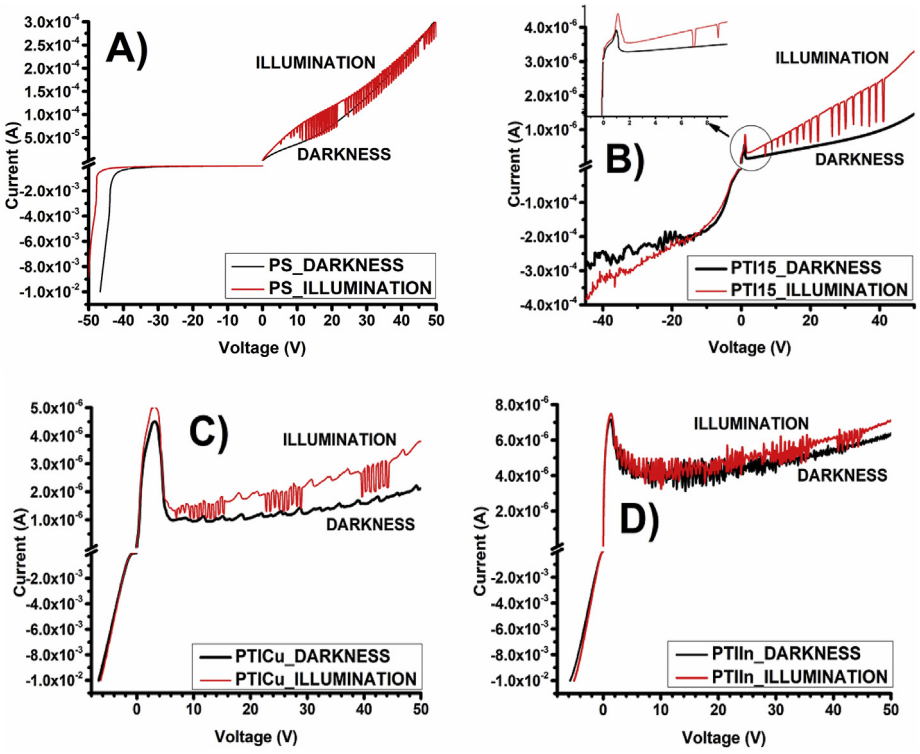

Fig. 8. Electrical behavior of the PS/TiO_2 structures a) Ni/PS/Si/Al b) PTI15 c) PTICu d) PTIIn.

experiments carried out by Du et al. [70], where they used TiO2 as an insulator between two electrodes, similar to the heterostructures proposed in this study.

However, the behavior of the Ni/TiO2: In/PS/Si/Al heterostructure could be associated with a Coulomb blockade, which has been associated with telegraph noise produced by trapping and de-trapping of carriers in trap states caused by the SiO2/Si interface and the diameter variation of silicon nanowires [66] since it is well-known that crystalline Si is oxidized rapidly in environmental conditions and the formation of PS layers generate the silicon nanowires with different diameters. Moreover, as mentioned above in the diffuse reflectance spectra analysis, the reduction of the bandgap is the result of the introduction of new energy levels (trap states) in the TiO2 bandgap, and thus, there is a high possibility of the NDR phenomenon taking advantage from the Coulomb blockade model.

For the Ni/TiO2: Cu/PS/Si/Al heterostructure there is not enough evidence to reach the same conclusion for the NDR origin since the wave-like effect appears in a periodic form; therefore, the telegraph noise effects from Coulomb blockade can be excluded. Thus, the charge storage could be related to this effect. The non-doped heterostructure could have two contributions, the first one could be the charge storage contributions due to the experiments in Ref. [70] and the second one would be the resonant tunneling due to the curves shown in this study, which show a fast exponential increase similar to the characteristic behavior for a conventional tunnel diode. Despite the models considered, it is not possible to account for the NDR effect from the lack of evidence, and this could be the topic for new research work.

On the other hand, the curves under illuminated conditions show a similar photoresponse when white light pulses are applied, as can be appreciated in Fig. 8b and c. However, in Fig. 8d, it is difficult to distinguish this photocurrent effect since there is not a significant difference between dark and light conditions.

Finally, it is important to note that the current is reduced two magnitude orders between the samples (with TiO2 film); this may be due to the high resistivity of the TiO2.

Moreover, all samples have shown a photocurrent signal, but the NDR effect only appears in the TiO2 film, which demonstrates that TiO2 is vital for this effect. Therefore, these structures can be used for different electronic applications, such as volatile memory devices [56].

4. Conclusions

This work has demonstrated the creation of nanostructures with important effects by using efficient synthetic methods. SEM characterization has revealed the morphology of the Ag nanoparticles before chemical etching. Also, the morphology of the PS layers showed a similar structure than that of the PS layers obtained by the electrochemical anodization process, which generates a reduction in the production cost. Depending on the dopant the TiO_2 structures showed unusual effects in the morphology, evident changes from nanoparticles (non-doped TiO_2) to complex micrometric structures similar to a cauliflower. Besides, the elemental analysis suggested a homogenous distribution of the dopant without the formation of Cu or In composites (Cu–O or In–O). Raman spectra showed the preference of the anatase phase with some peaks associated with the rutile phase without peaks associated with the formation of new composites related to the dopants. Moreover, other peaks found in the PS layers corresponded to silicon nanocrystals.

XRD diffractograms showed a combination of the anatase phase and the rutile phase, and by using the Sherrer equation, the crystal size was obtained with an evident increase with the dopants was calculated. PL spectra showed the behavior of the non-doped and doped heterostructures, and it was clear a passivation effect on the PS layer. Also, a variation in the intensity and a blue shifting due to the dopants were found. The origin of the PL was discussed, and it was stated that it could be originated from quantum confinement or structural defects on the surface of the PS layers; meanwhile, the luminescence of TiO_2 could be related to the oxygen vacancies, surface states or new level states introduced in the TiO_2 gap. Diffuse reflectance spectra were analyzed using the Kubelka-Munk method, and Urbach energy, a reduction of the bandgap was shown, and it was due to the dopant. This reduction was attributed to the new defect levels caused by the dopant elements.

Urbach energy gave an approximation of the level depth. Finally, electrical characterization of the heterostructures with TiO_2 showed surprising effects, since a negative differential resistance effect was observed in all samples. However, the origin of this effect is still unclear. Moreover, a photoresponse was found in all samples, which means that these kinds of structures could be used for specific applications in electronics or optoelectronics.

Declarations of interest

None.

AGR carried out the experimental set-up, the characterization and wrote the manuscript, C.Z.I and E.Q.G provided the idea and supervised the study. All authors read and approved the final manuscript.

Acknowledgments

The authors would like to thank CONACYT for its financial support through the scholarship number 568124.

References

[1] Barun Sarkar Mitra, Aniruddha Mondal, Bijit Choudhuri, Bikram Kishore Mahajan, Shubhro Chakrabartty, Chitralekh Ngangbam, Enlarged broad band photodetection using Indium doped TiO2 alloy thin film, J. Alloy. Comp. 615 (2014) 440–445 https://doi.org/10.1016/j.jallcom.2014.06.184.

[2] W. Zhao, W. Wang, X. Feng, L. He, Q. Cao, C. Luan, J. Ma, Preparation and characterization of transparent indium- doped TiO 2 films deposited by MOCVD, Ceram. Int. 43 (2017) 8391–8395, https://doi.org/10.1016/j.ceramint.2017.03.182.

[3] M. Yıldırım, Characterization of the framework of Cu doped TiO2 layers: an insight into optical, electrical and photodiode parameters, J. Alloy. Comp. 773 (2019) 890–904, https://doi.org/10.1016/j.jallcom.2018.09.276.

[4] E. Asadollahi, A.A. Youzbashi, M. Keyanpour-Rad, Synthesis and investigation of crystal structure and optical properties of brookite TiO2 nanoparticles capped with (2-chloroquinoline-3-yl) methanol, J. Mol. Struct. 1128 (2017) 612–618, https://doi.org/10.1016/j.molstruc.2016.09.032.

[5] M. Kumar, A.K. Gupta, D. Kumar, Mg-doped TiO2 thin films deposited by low cost technique for CO gas monitoring, Ceram. Int. 42 (2016) 405–410, https://doi.org/10.1016/j.ceramint.2015.08.124.

[6] Investigation of low temperature processed titanium dioxide (TiO2) films for printed dye sensitized solar cells (DSSCs) for large area flexible applications, Mater. Today: Proc. 5 (3) (2018) 13846–13854 https://doi.org/10.1016/j.matpr.2018.02.026.

[7] G. Zu, H. Li, S. Liu, D. Li, J. Wang, J. Zhao, Highly efficient mass determination of TiO2 nanotube arrays and its application in lithium-ion batteries, Sustain. Mater. Technol. (2018) e00079, , https://doi.org/10.1016/j.susmat.2018.e00079.

[8] E. Zalnezhad, A.M.S. Hamouda, G. Faraji, S. Shamshirband, TiO2 nanotube coating on stainless steel 304 for biomedical applications, Ceram. Int. 41 (2015) 2785–2793, https://doi.org/10.1016/j.ceramint.2014.10.098.

[9] Alexander Eibner, Action of light on pigments I, Chem. Ztg. 35 (1911) 753–755.

[10] W.H. Glaze, Drinking-water treatment with ozone, Environ. Sci. Technol. 21 (3) (1987) 224–230, https://doi.org/10.1021/es00157a001.

[11] W.H. Glaze, J.-W. Kang, D.H. Chapin, The chemistry of water treatment processes involving ozone, hydrogen peroxide and ultraviolet radiation, Ozone: Sci. Eng. 9 (4) (1987) 335–352, https://doi.org/10.1080/01919518708552148.

[12] M.A. Oturan, J.-J. Aaron, Advanced oxidation processes in water/wastewater treatment: principles and applications. A review, Crit. Rev. Environ. Sci. Technol. 44 (23) (2014) 2577–2641, https://doi.org/10.1080/10643389.2013.829765.

[13] S. Rahim Pouran, A.R. Abdul Aziz, W.M.A. Wan Daud, M.S. Shafeeyan, Effects of niobium and molybdenum impregnation on adsorption capacity and Fenton catalytic activity of magnetite, RSC Adv. 5 (106) (2015) 87535–87549, https://doi.org/10.1039/c5ra15660b.

[14] S. Rahim Pouran, A. Bayrami, A.R. Abdul Aziz, W.M.A. Wan Daud, M.S. Shafeeyan, Ultrasound and UV assisted Fenton treatment of recalcitrant wastewaters using transition metal-substituted-magnetite nanoparticles, J. Mol. Liq. 222 (2016) 1076–1084, https://doi.org/10.1016/j.molliq.2016.07.120.

[15] S. Rahim Pouran, A. Bayrami, A.A. Abdul Raman, W.M.A. Wan Daud, M.S. Shafeeyan, A. Khataee, Comprehensive study on the influence of molybdenum substitution on characteristics and catalytic performance of magnetite nanoparticles, Res. Chem. Intermed. 44 (2) (2017) 883–900, https://doi.org/10.1007/s11164-017-3142-x.

[16] M.R. Delsouz Khaki, M.S. Shafeeyan, A.A.A. Raman, W.M.A.W. Daud, Evaluating the efficiency of nano-sized Cu doped TiO2/ZnO photocatalyst under visible light irradiation, J. Mol. Liq. 258 (2018) 354–365, https://doi.org/10.1016/j.molliq.2017.11.030.

[17] M. Ge, J. Cai, J. Iocozzia, C. Cao, J. Huang, X. Zhang, J. Shen, S. Wang, S. Zhang, K.-Q. Zhang, Y. Lai, Z. Lin, A review of TiO 2 nanostructured catalysts for sustainable H 2 generation, Int. J. Hydrogen Energy 42 (2017) 8418–8449, https://doi.org/10.1016/j.ijhydene.2016.12.052.

[18] D.D. Marco, K. Drissi, P.M. Geffroy, N. Delhote, O. Tantot, S. Verdeyme, T. Chartier, Dielectric properties of alumina doped with TiO2 from 13 to 73 GHz, J. Eur. Ceram. Soc. 37 (2017) 641–646, https://doi.org/10.1016/j.jeurceramsoc.2016.09.016.

[19] N.N. Bao, J.B. Yi, H.M. Fan, X.B. Qin, P. Zhang, B.Y. Wang, J. Ding, S. Li, Vacancy induced room-temperature ferromagnetism in Ga-TiO2, Scr. Mater. 66 (2012) 821–824, https://doi.org/10.1016/j.scriptamat.2012.02.031.

[20] Y. Gao, S. Thevuthasan, D.E. McCready, M. Engelhard, MOCVD growth and structure of Nb- and V-doped TiO2 films on sapphire, J. Cryst. Growth 212 (2000) 178–190, https://doi.org/10.1016/s0022-0248(00)00010-5.

[21] E.M. Samsudin, S.B. Abd Hamid, J.C. Juan, W.J. Basirun, A.E. Kandjani, S.K. Bhargava, Controlled nitrogen insertion in titanium dioxide for optimal photocatalytic degradation of atrazine, RSC Adv. 5 (2015) 44041–44052, https://doi.org/10.1039/C5RA00890E.

[22] W. Choi, A. Termin, M.R. Hoffmann, The role of metal ion dopants in quantum-sized TiO2: correlation between photoreactivity and charge carrier recombination dynamics, J. Phys. Chem. C 98 (1994) 13669–13679, https://doi.org/10.1021/j100102a038.

[23] N.A. Al Saqri, A. Mondal, J.F. Felix, Y.G. Gobato, V.O. Gordo, H. Albalawi, D. Jameel, H. Alghamdi, F. Al Mashary, D. Taylor, M.S. Abd El-sadek, M. Henini, Investigation of defects in indium doped TiO2 thin films using electrical and optical techniques, J. Alloy. Comp. 698 (2017) 883–891, https://doi.org/10.1016/j.jallcom.2016.12.294.

[24] Biswajit Choudhury, Munmun Dey, Amarjyoti Choudhury, Defect generation, d-d transition, and band gap reduction in Cu-doped TiO2 nanoparticles, Int. Nano Lett. 3 (2013) 25, https://doi.org/10.1186/2228-5326-3-25.

[25] M.R. Delsouz Khaki, M.S. Shafeeyan, A.A.A. Raman, W.M.A.W. Daud, Enhanced UV–Visible photocatalytic activity of Cu-doped ZnO/TiO2 nanoparticles, J. Mater. Sci. Mater. Electron. 29 (7) (2018) 5480–5495, https://doi.org/10.1007/s10854-017-8515-9.

[26] S. Sampath, P. Maydannik, T. Ivanova, M. Shestakova, T. Homola, A. Bryukvin, ... V. Alagan, Efficient solar photocatalytic activity of TiO2 coated nano-porous silicon by atomic layer deposition, Superlattice Microstruct. 97 (2016) 155–166, https://doi.org/10.1016/j.spmi.2016.06.004.

[27] J. Castañeda-Contreras, V.F. Marañón-Ruiz, R. Chiu-Zárate, H. Pérez-Ladrón de Guevara, R. Rodriguez, C. Michel-Uribe, Photocatalytic activity of erbium-doped TiO2 nanoparticles immobilized in macro-porous silica films, Mater. Res. Bull. 47 (2012) 290–295, https://doi.org/10.1016/j.materresbull.2011.11.021.

[28] Y.S. Sakhare, S.V. Bhoraskar, V.L. Mathe, A.U. Ubale, Electric field assisted enhanced photo catalytic activities of immobilized nano TiO 2 on porous silicon, Mater. Res. Bull. 59 (2014) 205–213, https://doi.org/10.1016/j.materresbull.2014.07.006.

[29] A. Uhlir, Electrolytic shaping of germanium and silicon, Bell Tech. J. 35 (1956) 333–347, https://doi.org/10.1002/j.1538-7305.1956.tb02385.x.

[30] L.T. Canham, Silicon quantum wire array fabrication by electrochemical and chemical dissolution of wafers, Appl. Phys. 57 (1990) 1046–1048, https://doi.org/10.1063/1.103561.

[31] A.I. Manilov, V.A. Skryshevsky, Hydrogen in porous silicon A review, Mater. Sci. Eng., B 178 (2013) 942–955, https://doi.org/10.1016/j.mseb.2013.05.001.

[32] C. Roy Chaudhuri, A review on porous silicon based electrochemical biosensors: beyond surface area enhancement factor, Sens. Actuators B Chem. 210 (2015) 310–323, https://doi.org/10.1016/j.snb.2014.12.089.

[33] N. Baran, H. Gebavi, L. Mikac, D. Ristić, M. Gotić, K. Syed, M. Ivanda, Sensing properties of oxidized nanostructured silicon surface on vaporized molecules, Sensors 19 (2019) 119, https://doi.org/10.3390/s19010119.

[34] Shiping Xu, Xiang Sun, Yuan Gao, Min Yue, Qinyan Yue, Baoyu Gao, Solvent effects on microstructures and properties of three-dimensional hierarchical TiO_2 microsphere structures synthesized via solvothermal approach, J. Solid State Chem. 253 (2017) 167–175, https://doi.org/10.1016/j.jssc.2017.05.001.

[35] M.K. Ahmad, S.M. Mokhtar, C.F. Soon, N. Nafarizal, A.B. Suriani, A. Mohamed, M.H. Mamat, M.F. Malek, M. Shimomura, K. Murakami, Raman investigation of rutile-phased TiO_2 nanorods/nanoflowers with various reaction times using one step hydrothermal method, J. Mater. Sci. Mater. Electron. 27 (2016) 7920–7926, https://doi.org/10.1007/s10854-016-4783-z.

[36] K. Farhadian Azizi, M.-M. Bagheri-Mohagheghi, Transition from anatase to rutile phase in titanium dioxide (TiO2) nanoparticles synthesized by complexing sol–gel process: effect of kind of complexing agent and calcinating temperature, J. Sol. Gel Sci. Technol. 65 (2013) 329–335, https://doi.org/10.1007/s10971-012-2940-2.

[37] C.Y. Wang, et al., Thermal annealing effects study on electrical and structural properties for Ni-Au/n-GaN Schottky contacts, Appl. Mech. Mater. 284–287 (2013) 241–244.

[38] Z. Huang, N. Geyer, P. Werner, J. de Boor, U. Gösele, Metal-Assisted chemical etching of silicon: a review, Adv. Mater. 23 (2) (2010) 285–308, https://doi.org/10.1002/adma.201001784.

[39] E. Quiroga-González, M.Á. Juárez-Estrada, E. Gómez-Barojas, (Invited) light enhanced metal assisted chemical etching of silicon, ECS Trans. 86 (2018) 55–63, https://doi.org/10.1149/08601.0055ecst.

[40] D.H. Everett, IUPAC, manual of symbol and terminology for physico -chemical quantities and units, appendix, definitions, terminology and symbols in colloid and surface chemistry, Part I, Pure Appl. Chem. 31 (1972) 579–638, https://doi.org/10.1351/pac197231040577.

[41] Woo-Jin Lee, Yong-Ho Choa, Highly conformal carbon-doped SiCN films by plasma-enhanced chemical vapor deposition with enhanced barrier properties, Thin Solid Films 657 (2018) 32–37, https://doi.org/10.1016/j.tsf.2018.04.042.

[42] A. Augustin, K. Rajendra Udupa, K. Udaya Bhat, Effect of coating current density on the wettability of electrodeposited copper thin film on aluminum substrate, Perspect. Sci. 8 (2016) 472–474, https://doi.org/10.1016/j.pisc.2016.06.003.

[43] Patricia M. Perillo, Daniel F. Rodriguez, Growth control of TiO_2 nanotubes in different physical environments, Nanosci. Methods 1 (2012) 194–200, https://doi.org/10.1080/17458080.2012.663507.
[44] Priyanka Dwivedia, Neha Chauhanb, P. Vivekanandanb, Samaresh Dasa, D. Sakthi Kumarb, Saakshi Dhanekara, Scalable fabrication of prototype sensor for selective and sub-ppmlevel ethanol sensing based on TiO_2 nanotubes decorated porous silicon, Sens. Actuators B 249 (2017) 602–610, https://doi.org/10.1016/j.snb.2017.03.154.
[45] M. Lubas, J.J. Jasinski, M. Sitarz, L. Kurpaska, P. Podsiad, J. Jasinski, Raman Spectroscopy of TiO_2 thin films formed by hybrid treatment for biomedical applications, Spectrochim. Acta A Mol. Biomol. Spectrosc. 133 (2014) 867–871, https://doi.org/10.1016/j.saa.2014.05.045.
[46] X. Xue, W. Ji, Z. Mao, H. Mao, Y. Wang, X. Wang, W. Ruan, B. Zhao, J.R. Lombardi, Raman investigation of nanosized TiO2: effect of crystallite size and phonon confinement, J. Phys. Chem. C 116 (2012) 8792–8797, https://doi.org/10.1021/jp2122196.
[47] F.S. Al mashary, S. de Castro, A.F. da Silva, J.F. Felix, M.R. Piton, Helder.Viní.Avanç Galeti, A. De Giovanni Rodrigues, Yara.Galvã. Gobato, N. Al Saqri, M. Henini, M.M. Al huwayz, A.M. Albadri, A.Y. Alyamani, H.A. Albrathen, S.A. Alhusaini, K.M. Aljaber, A.Z. Alanazi, F.S. Alghamdi, Effect of growth techniques on the structural, optical and electrical properties of indium doped TiO2 thin films, J. Alloy. Comp. 766 (2018) 194–203, https://doi.org/10.1016/j.jallcom.2018.06.360.
[48] Z. Lan, Y. Yu, S. Yan, E. Wang, J. Yao, Y. Cao, Synergetic effect of N 3−, in 3+ and Sn 4+ ions in TiO2 towards efficient visible photocatalysis, J. Photochem. Photobiol. A Chem. 356 (2018) 132–137, https://doi.org/10.1016/j.jphotochem.2017.12.032.
[49] Muhammad Tahir, Nor Aishah Saidina Amin, Indium-doped TiO2nanoparticles for photocatalytic CO2 reduction with H2O vapors to CH4, Appl. Catal. B Environ. 162 (2015) 98–109, https://doi.org/10.1016/j.apcatb.2014.06.037.
[50] M. Tahir, N.S. Amin, Photocatalytic CO2 reduction with H2 as reductant over copper and indium co-doped TiO2 nanocatalysts in a monolith photoreactor, Appl. Catal. Gen. 493 (2015) 90–102, https://doi.org/10.1016/j.apcata.2014.12.053.
[51] K.-R. Zhu, M.-S. Zhang, J.-M. Hong, Z. Yin, Size effect on phase transition sequence of TiO2 nanocrystal, Mater. Sci. Eng. A 403 (2005) 87–93, https://doi.org/10.1016/j.msea.2005.04.029.
[52] Leigh Canham, Knovel (Firm), Properties of Porous Silicon, Institution of Electrical Engineers, London, 1997.
[53] A.G. Nassiopoulou, H.S. Nalwa (Ed.), Encyclopedia of Nanoscience and Nanotechnology, Silicon Nanocrystals and Nanowires Embedded in SiO_2, American Scientific Publishers, California, 2004 793–813.
[54] H. Mizuno, H. Koyama, N. Koshida, Oxide-free blue photoluminescence from photochemically etched porous silicon, Appl. Phys. Lett. 8 (1996) 3779, https://doi.org/10.1063/1.116996.
[55] M. Wolkin, J. Jorne, P. Fauchet, G. Allan, C. Delerue, Electronic states and luminescence in porous silicon quantum dots: the role of oxygen, Phys. Rev. Lett. 8 (1999) 197–200, https://doi.org/10.1103/PhysRevLett.82.197.
[56] E. Lioudakis, A. Othonos, A.G. Nassiopoulou, Ultrafast transient photoinduced absorption in silicon nanocrystals: coupling of oxygen-related states to quantized sublevels, Appl. Phys. Lett. 8 (2007) 171103, https://doi.org/10.1063/1.2728756.
[57] Ioannis Leontis, Andreas Othonos, Androula G. Nassiopoulou, Structure, morphology, and photoluminescence of porous Si nanowires: effect of different chemical treatments, Nanoscale Res. Lett. 8 (2013) 383, https://doi.org/10.1186/1556-276X-8-383.
[58] L.T. Cong, N.T. Ngoc Lam, N.T. Giang, P.T. Kien, N.D. Dung, N.N. Ha, N-type silicon nanowires prepared by silver metal-assisted chemical etching: fabrication and optical properties, Mater. Sci. Semicond. Process. 90 (2019) 198–204, https://doi.org/10.1016/j.mssp.2018.10.026.
[59] G.D. Sanders, Y.C. Chang, Theory of optical properties of quantum wires in porous silicon, Phys. Rev. B 45 (1992) 9202–9213, https://doi.org/10.1103/physrevb.45.9202.
[60] K.W. Cheah, T. Chan, W.L. Lee, D. Teng, W.H. Zheng, Q.M. Wang, Multiple peak photoluminescence of porous silicon, Appl. Phys. Lett. 63 (1993) 3464–3466, https://doi.org/10.1063/1.110121 1993.
[61] M.V. Wolkin, J. Jorne, P.M. Fauchet, G. Allan, C. Delerue, Electronic states and luminescence in porous silicon quantum dots: the role of oxygen, Phys. Rev. Lett. 82 (1999) 197–200, https://doi.org/10.1103/physrevlett.82.197.
[62] T.T. Loan, V.H. Huong, V.T. Tham, N.N. Long, Effect of zinc doping on the bandgap and photoluminescence of Zn 2+ -doped TiO 2 nanowires, Phys. B Condens. Matter 532 (2018) 210–215, https://doi.org/10.1016/j.physb.2017.05.027 2018.
[63] F. Labreche, A. Berbadj, N. Brihi, R. Karima, B. Jamoussi, Green photoluminescence, structural and optical properties of Nd-TiO 2 thin films, Optik 172 (2018) 63–71, https://doi.org/10.1016/j.ijleo.2018.06.131.
[64] Snehamol Mathew, Priyanka Ganguly, Stephen Rhatigan, Vignesh Kumaravel, Ciara Byrne, Steven Hinder Hinder, John Bartlett, Michael Nolan, Suresh Pillai, Cu doped TiO2: visible light assisted photocatalytic antimicrobial activity and high temperature anatase stability. ChemRxiv, Preprint, 2018. https://doi.org/10.26434/chemrxiv.7159733.v1.
[65] T.Z. Al-Tayyar, N.A. Salman, Impact of the variability in the current density on the porous silicon characteristics, Energy Procedia 50 (2014) 488–493, https://doi.org/10.1016/j.egypro.2014.06.059.
[66] O. Marin, V. Toranzos, R. Urteaga, D. Comedi, R.R. Koropecki, Negative differential resistance in porous silicon devices at room temperature, Superlattice Microstruct. 79 (2015) 45–53, https://doi.org/10.1016/j.spmi.2014.12.019.
[67] L. Esaki, New phenomenon in narrow germanium p-n junctions, Phys. Rev. 109 (1958) 603–604, https://doi.org/10.1103/physrev.109.603.
[68] V. Nam Do, P. Dollfus, Negative differential resistance in zigzag-edge graphene nanoribbon junctions, J. Appl. Phys. 107 (2010) 063705, https://doi.org/10.1063/1.3340834.
[69] T. Rakshit, G.-C. Liang, A.W. Ghosh, S. Datta, Silicon-based molecular electronics, Nano Lett. 4 (2004) 1803–1807, https://doi.org/10.1021/nl049436t.
[70] Y. Du, H. Pan, S. Wang, T. Wu, Y.P. Feng, J. Pan, A.T.S. Wee, Symmetrical negative differential resistance behavior of a resistive switching device, ACS Nano 6 (2012) 2517–2523, https://doi.org/10.1021/nn204907t.